VU Research Portal

Paratethys pacing of the Messinian Salinity Crisis

Grothe, Arjen; Andreetto, Federico; Reichart, Gert Jan; Wolthers, Mariette; Van Baak, Christiaan G.C.; Vasiliev, Iuliana; Stoica, Marius; Sangiorgi, Francesca; Middelburg, Jack J.; Davies, Gareth R.; Krijgsman, Wout

Link to publication in VU Research Portal

Paratethys pacing of the Messinian Salinity Crisis: Low salinity waters contributing to gypsum precipitation?

Arjen Grothe [a], Federico Andreetto [a], Gert-Jan Reichart [a,b], Mariette Wolthers [a], Christiaan G.C. Van Baak [a,c], Iuliana Vasiliev [d], Marius Stoica [e], Francesca Sangiorgi [a], Jack J. Middelburg [a], Gareth R. Davies [f], Wout Krijgsman [a,*]

[a] Department of Earth Sciences, Utrecht University, Princetonlaan 8A, 3584 CB, Utrecht, the Netherlands
[b] Royal Netherlands Institute for Sea Research (NIOZ), 1790 AB Den Burg, Texel, and Utrecht University, the Netherlands
[c] CASP, West Building, Madingley Rise, Madingley Road, Cambridge CB3 0UD, UK
[d] Senckenberg Biodiversity and Climate Research Centre, Senckenberganlage 25, 60325, Frankfurt am Main, Germany
[e] Department of Geology, University of Bucharest, Bălcescu Bd. 1, Bucharest, 010041, Romania
[f] Geology & Geochemistry, VU University, De Boelelaan 1085, 1081 HV, Amsterdam, the Netherlands

ARTICLE INFO

ABSTRACT

During the so-called Messinian Salinity Crisis (MSC: 5.97-5.33 Myr ago), reduced exchange with the Atlantic Ocean caused the Mediterranean to develop into a "saline giant" wherein ∼1 million km^3 of evaporites (gypsum and halite) were deposited. Despite decades of research it is still poorly understood exactly how and where in the water column these evaporites formed. Gypsum formation commonly requires enhanced dry conditions (evaporation exceeding precipitation), but recent studies also suggested major freshwater inputs into the Mediterranean during MSC-gypsum formation. Here we use strontium isotope ratios of ostracods to show that low-saline water from the Paratethys Seas actually contributed to the precipitation of Mediterranean evaporites. This apparent paradox urges for an alternative mechanism underlying gypsum precipitation. We propose that Paratethys inflow would enhance stratification in the Mediterranean and result in a low-salinity surface-water layer with high Ca/Cl and SO$_4$/Cl ratios. We show that evaporation of this surface water can become saturated in gypsum at a salinity of ∼40, in line with salinities reported from fluid inclusions in MSC evaporites.

© 2019 Elsevier B.V. All rights reserved.

1. Introduction

The deposition of salts ("evaporites") on Earth is generally associated with hydrographically isolated basins in evaporative environments (Warren, 2010). By ongoing evaporation, sea water salinity increases and ultimately saturation with respect to certain minerals causes mineral deposition. The most common evaporite, gypsum ($CaSO_4 \cdot 2H_2O$), forms in waters that are 4 to 5 times more concentrated in salts than average seawater: ∼130-160 g/l (Warren, 2010).

Occasionally in Earth's history, evaporite deposition took place at large scale in so-called "saline giants". Earth's most recent saline giant occurred in the Mediterranean Basin during the late Miocene (Hsü et al., 1973; Ryan, 2009). Restriction of seawater exchange between the (proto) Mediterranean Sea and the Atlantic Ocean cul-

minated in the so-called Messinian Salinity Crisis (MSC) between 5.97-5.33 Ma (Roveri et al., 2014a; Flecker et al., 2015). The MSC is subdivided into three main stages, all characterized by specific environmental conditions (Roveri et al., 2014a). MSC Stage 1 (5.97-5.6 Myr ago) is marked by rhythmic alternations of marine marls and gypsum in the shallow basins, while the Mediterranean remained connected to the Atlantic Ocean. During MSC Stage 2 (5.6-5.55 Myr ago), the most saline conditions were reached and halite formed in the deeper basins. MSC Stage 3 (5.55-5.33 Myr ago) is characterized by large temporal salinity differences; both rhythmic gypsum-marl couplets and evaporite-free fresh to brackish water deposits occur.

Fundamental questions remain about the trigger for gypsum formation and where in the water column it formed (De Lange and Krijgsman, 2010; Lugli et al., 2010). Classically, MSC-gypsum formation is considered to result from enhanced (seasonal) drought during precession maxima (Krijgsman et al., 2001; Topper and Meijer, 2013; Topper et al., 2014; Roveri et al., 2014b). Stable
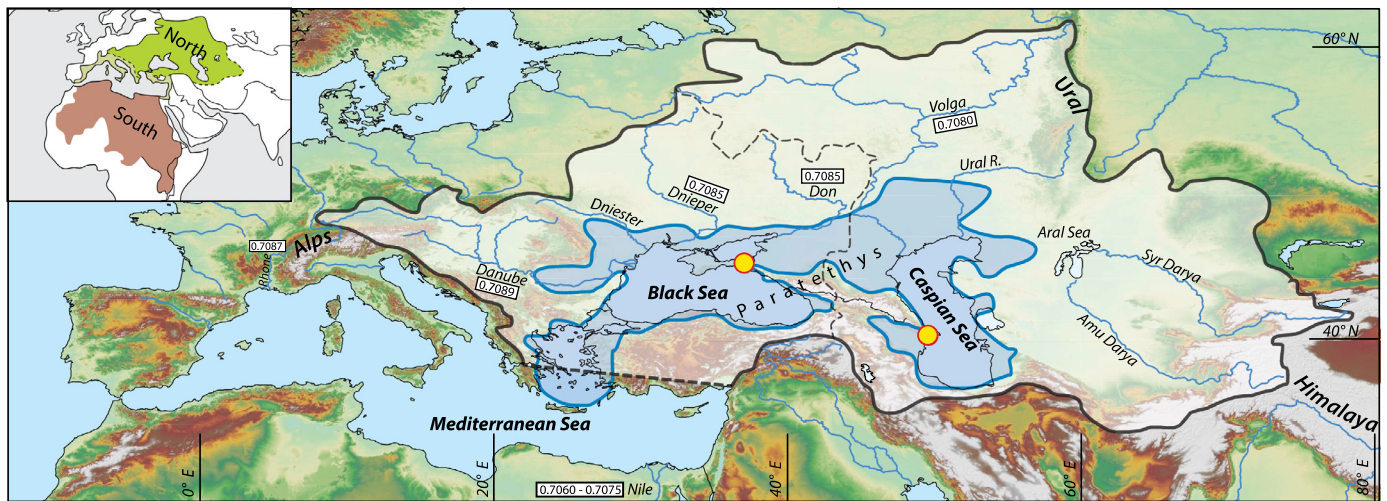
Fig. 1. Elevation map showing the extent of the late Miocene Black and Caspian Sea and their drainage basins. The former Paratethys Sea during the latest Miocene is outlined according to Popov et al. (2006). These authors consider the Aegean domain as an intermittent region between Mediterranean and Paratethys. Yellow dots indicate the studied sections; Zheleznyi Rog (Russia) and Adzhiveli (Azerbaijan). The main rivers are labelled with their modern $^{87}Sr/^{86}Sr$ ratios. The areal distribution of the two main water sources, northern (European) and southern (African) rivers draining into the Mediterranean-Paratethys system, is presented in the inset. (For interpretation of the colours in the figure(s), the reader is referred to the web version of this article.)

Table 1
Present-day strontium values of major Paratethyan and Mediterranean fresh water sources.

| River	Q (km³/yr)	Sr conc. (μmol/kg)	Sr flux	$^{87}Sr/^{86}Sr$	Source
Danube	207	2.76	5.71×10^8	0.7089	Palmer and Edmond, 1989
Dnieper	43	2.50	1.08×10^8	0.7084	Palmer and Edmond, 1989
Don	26	2.50	6.50×10^7	0.7084	Palmer and Edmond, 1989
Volga	239.7	5.48	1.31×10^9	0.708083	Clauer et al., 2000 Kroonenberg et al., 2011
Hydrothermal vents	~14.6	~106	~1.55×10^9	0.70821	Clauer et al., 2000
Mediterranean seawater stage 1	–	87.0?	–	~0.7089-0.7090[*]	Roveri et al., 2014a, 2014b Broecker and Peng, 1982
Nile	–	–	1.56×10^8	0.706-0.7071	Brass, 1976 Gerstenberger et al., 1997
Rhone	55	5.94	3.27×10^8	0.7087	Palmer and Edmond, 1989
Atlantic inflow	22706	87.0	1.97×10^{12}	~0.7090[*]	Broecker and Peng, 1982 Bryden et al., 1994
Black Sea inflow	300	–	–	–	Jarosz et al., 2013
Black Sea outflow	400	–	–	–	Jarosz et al., 2013

[*] Messinian Salinity Crisis-values.

isotope analyses of gypsum hydration water and the salinity of fluid inclusions in MSC-gypsum, however, indicate large freshwater inputs during gypsum formation in both Stage 1 (Natalicchio et al., 2014; Evans et al., 2015) and Stage 3 (Costanzo et al., 2019). Freshwater inputs were initially attributed to Mediterranean rivers (Fig. 1 and Table 1), because the adjacent Black Sea was thought to have desiccated during the MSC (Hsü and Giovanoli, 1980; Gillet et al., 2007). Recent paleoenvironmental reconstructions, however, demonstrated that the Black and Caspian Seas remained water-filled and had a positive hydrological budget throughout the MSC (Grothe et al., 2014; Marzocchi et al., 2016; Van Baak et al., 2017). They were unified in the large Paratethys Sea (Fig. 1), which provided a potential source for low-salinity waters to the Mediterranean (Krijgsman et al., 2010; Van Baak et al., 2015).

Episodic freshwater input into the Mediterranean is important, as it will have affected saturation state with respect to different minerals. Radiogenic strontium isotope ratios ($^{87}Sr/^{86}Sr$) are potentially a powerful tracer of Mediterranean water sources (Flecker and Ellam, 2006; Topper et al., 2014). In restricted basins, the $^{87}Sr/^{86}Sr$ ratio is offset from coeval ocean water signatures and controlled by mixing with non-marine Sr sources such as hydrothermal vents and river waters (Vasiliev et al., 2010; Roveri et al., 2014b; Reghizzi et al., 2017). These regional inputs have char-

acteristic isotopic compositions and concentrations reflecting the lithology of the hinterland. During the MSC, the Mediterranean represents an archetype of a strongly restricted basin. The progressive shift from pre-MSC marine values (~0.7090) to lower values (down to 0.7085 during MSC Stage 3) (Fig. 2) is considered a further proof of the increasing deterioration of the Atlantic connection, accompanied by an increased sensitivity to continental runoff (Roveri et al., 2014b; Reghizzi et al., 2018). This provides the Mediterranean low radiogenic Sr in accordance with the Rb-depleted Mesozoic carbonates and Cenozoic basalts forming the catchment of the main peri-Mediterranean rivers (Brass, 1976; Gerstenberger et al., 1997). The role of Paratethyan waters in explaining these deviations remains uncertain as $^{87}Sr/^{86}Sr$ data from the late Messinian Paratethys are lacking (Vasiliev et al., 2010).

To test whether input of Paratethyan waters into the Mediterranean potentially governed the MSC, we determined late Miocene $^{87}Sr/^{86}Sr$ ratios of the Black and Caspian waters by measuring $^{87}Sr/^{86}Sr$ ratios of calcareous ostracod shells. Calcareous organisms incorporate Sr directly into their shell, thereby representing a proxy of the isotopic composition of the water they lived in (Flecker and Ellam, 2006). To reconstruct the strontium isotope composition ($^{87}Sr/^{86}Sr$) of the Paratethys Sea during the MSC, we used ostracods from two outcrop sections: Zheleznyi Rog (Black
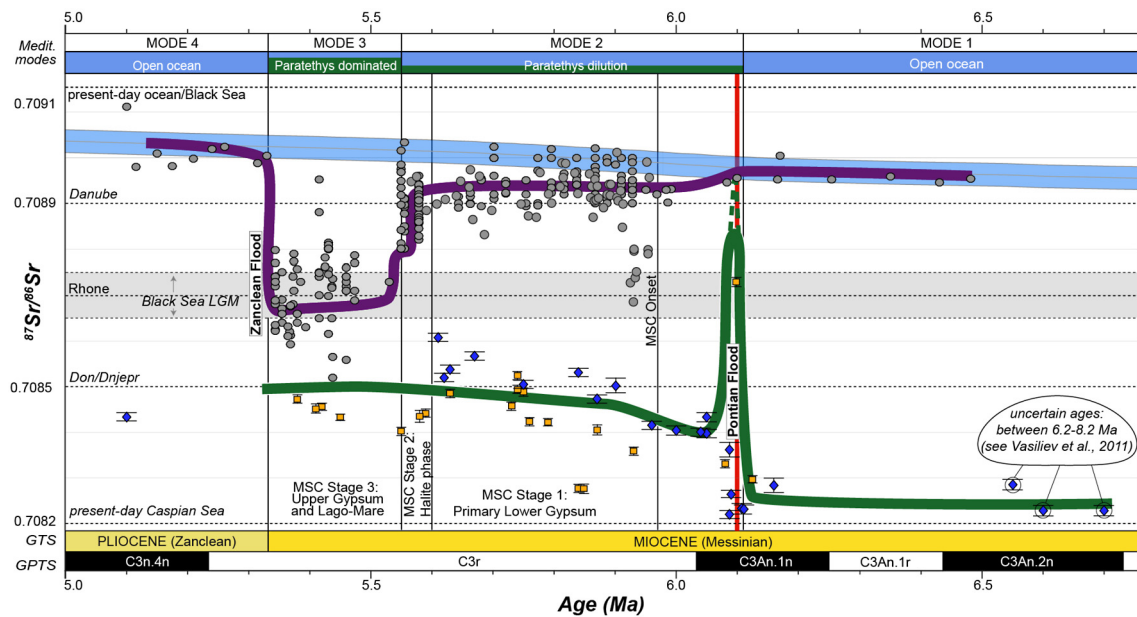
Fig. 2. Late Miocene-earliest Pliocene $^{87}Sr/^{86}Sr$ data for the Mediterranean (grey circles), Black (blue diamonds) and Caspian (orange squares) Seas. Mediterranean and oceanic (blue shaded band) $^{87}Sr/^{86}Sr$ data are derived from various sources; see Roveri et al. (2014a) for an overview. Green and purple lines indicate our interpretation of the $^{87}Sr/^{86}Sr$ ratio trend of the Black and Caspian Sea combined, and the Mediterranean, respectively. Samples predating ∼6.2 Ma have large age-uncertainties because of several hiatuses in the Maeotian part of the section (Vasiliev et al., 2011). Dashed lines indicate the $^{87}Sr/^{86}Sr$ of the Danube, Don, Dnieper, Rhone rivers, and the present-day Caspian and Black Seas. $^{87}Sr/^{86}Sr$ of Nile (0.706-0.7071) and Volga (0.708083) are not plotted. Grey shaded zone indicates $^{87}Sr/^{86}Sr$ ratios of the Black Sea during last glacial maximum (LGM). Messinian Salinity Stages 1-3 are labelled and Global Time Scale (GTS) and Geomagnetic Polarity Time Scale (GPTS) are shown at the bottom.

Sea) and Adzhiveli (Caspian Sea) (Vasiliev et al., 2011; Van Baak et al., 2016).

2. Sections in the Paratethys

The Black and Caspian Seas were, since the Oligocene, part of the large epicontinental Paratethys Sea (Fig. 1), which covered large parts of Eurasia stretching from Germany to Tajikistan (Popov et al., 2006). Due to restricted conditions, endemic fauna developed, which form the basis for regional stratigraphic correlation. The MSC corresponds in the Black Sea to the regional Pontian Stage and part of the Kimmerian Stage (Krijgsman et al., 2010). In the Caspian region, it includes the entire Pontian Stage (Van Baak et al., 2016). The Pontian Stage is preceded by the Maeotian Stage and succeeded by the Kimmerian Stage (Black Sea) and the Productive Series (Caspian Sea).

The ∼500-m-thick Zheleznyi Rog section (45°06.9082′N, 36°45.646′E), comprises ca. 5 Myr of sediments and is one of the most extensively studied Neogene successions of the Black Sea Basin (Popov et al., 2006, 2016; Krijgsman et al., 2010; Vasiliev et al., 2011; Stoica et al., 2016). The deposits of the upper Maeotian comprise grey clays and whitish diatomites, while alternations of grey marls and whitish diatomite layers characterize the Pontian. The onset of the Kimmerian Stage (ca. 5.6 Ma) is marked by an iron-rich layer of oolithic sandstone that may represent a hiatus (Krijgsman et al., 2010; Vasiliev et al., 2011). On top of this red bed, dark grey marls with interbedded limonite-rich layers mark the Kimmerian. Age constraints were provided by magnetostratigraphy coupled with biostratigraphy (ostracods, mollusks), event stratigraphy (foraminifera) and $^{40}Ar/^{39}Ar$ ages (Vasiliev et al., 2011).

The Adzhiveli section (40°18.440′N, 49°4.211′E) is a 130 m thick section located in central Azerbaijan (Fig. 1). The section spans the upper Maeotian and Pontian Stages. The deposits comprise (silty) clays and marls that alternate in colour between brownish grey and dark grey (Van Baak et al., 2016). The lower part of the section includes some diatomitic beds. Marine sedi-

ments at the base of the section yield foraminifera and radiolarians that correspond to the Pontian Flooding. Based on magneto- and cyclostratigraphy coupled with biostratigraphy (ostracods) and event stratigraphy (foraminifera), this section spans roughly from ∼6.16 Ma to <5.38 Ma (Van Baak et al., 2016).

3. Methods

3.1. Sample preparation

All $^{87}Sr/^{86}Sr$ analyses were performed on handpicked ostracods that were separated from the bulk sediment by disaggregation in sodium carbonate solution and wet sieving to retain the >250 μm fraction. The ostracod samples were not crushed prior to the cleaning procedure. Clays were removed by washing five times in MilliQ®, five times in methanol (96%) and by ∼5-30 s cleaning in an ultrasonic bath.

3.2. Diagenetic evaluation

Selected cleaned samples were evaluated for potential diagenetic alteration using trace element profiling of the shells and scanning electron microscopy (SEM; Fig. 3). Ostracod shells from Zheleznyi Rog were ablated using a Lambda Physik Excimer 193 nm laser with GeoLas 200Q optics coupled to a Micromass Platform quadrupole ICP-MS at Utrecht University. Ablation was performed in a mixed atmosphere of helium and argon with a repetition rate of 6 Hz and spot diameter of 80 μm. Calibration was performed against U.S. National Institute of Standards and Technology SRM 610 glass using the concentration data of Jochum et al. (2011) with ^{44}Ca as an internal standard. To reduce spectral interferences of the minor Ca isotopes (^{42}Ca, ^{43}Ca, ^{44}Ca), a collision and reduction cell was used (Mason and Kraan, 2002).

Samples from Adzhiveli (Caspian Sea) were ablated in a He environment using a NWR193UC (New Wave Research) laser, containing a 193 nm short pulse ArF Excimer laser, coupled to a quadrupole ICP-MS (Thermo Scientific iCAP-Q) at the Royal NIOZ.
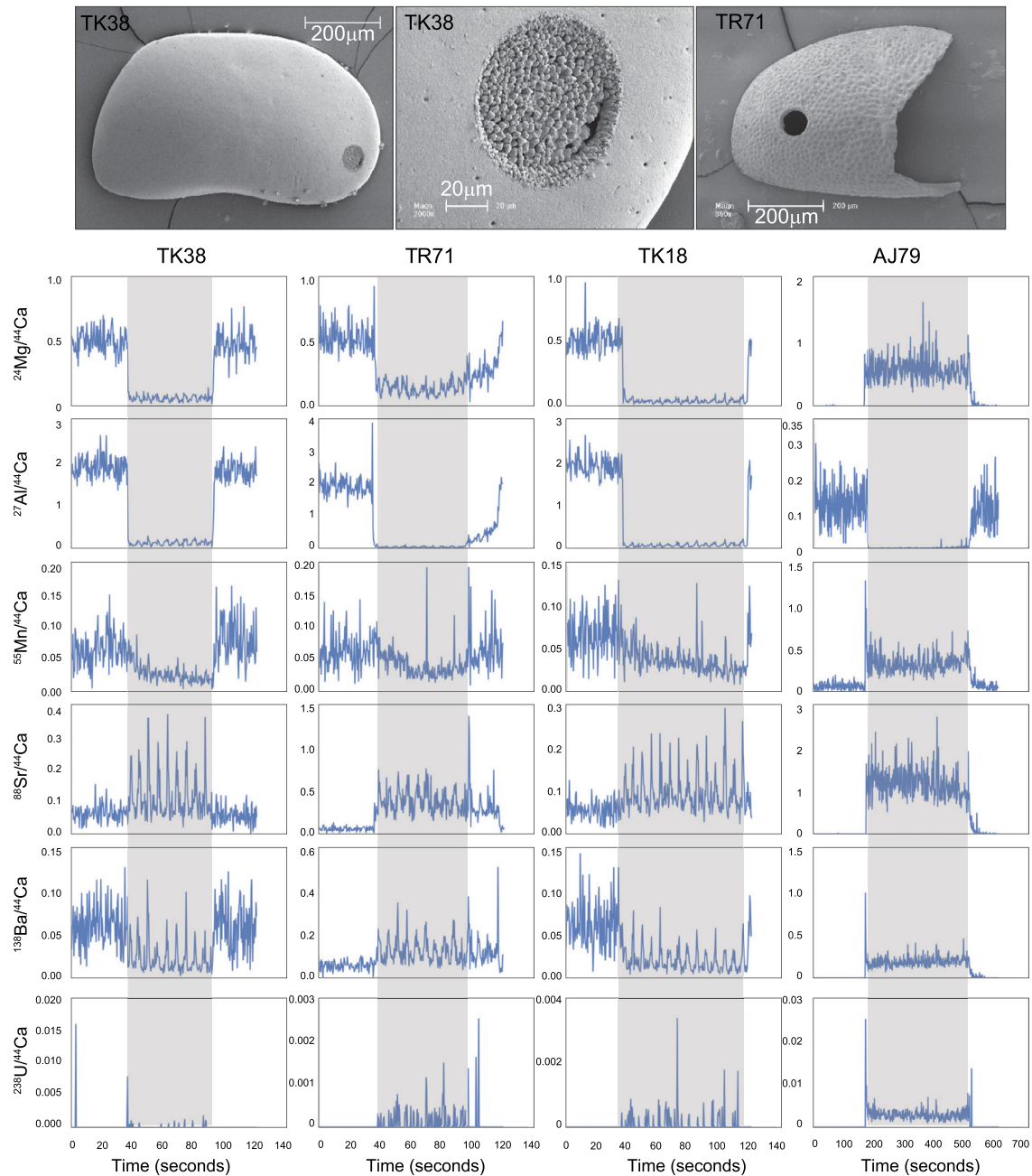
Fig. 3. Scanning electron micrograph of two ostracods species from the Zheleznyi Rog-section (*Caspiocypris atta* (TK38) and *Cyprideis* sp. (TR71)) with the ablation craters. Time resolved laser-ablation inductively coupled plasma-mass spectrometry data is shown for four representative samples. Values are normalized against ^{44}Ca to correct for variations in ablation rates. Typically, material is ablated at different rates causing a variation in counts per second. Some peaks on the outside of the shell, e.g. ^{27}Al/^{44}Ca of TR71 or ^{55}Mn/^{44}Ca of AJ79, indicate some clay minerals and/or coating that were not removed despite the cleaning procedure. However, the relative contribution of this outside contamination is very low. The Sr counts in the contamination peak of AJ79 account only for <0,1% of the ^{88}Sr content of the entire shell. Furthermore, all ratios show a stable signal without appreciable peaks inside the shell indicating pristine preservation. Hence, post-depositional alternation of the isotopes due to secondary processes can therefore be excluded. The non-contaminated part of the ostracods shells is marked by the grey interval.

Laser ablation was performed with an energy density of approximately 1 J/cm^2 and at a repetition rate of 6 Hz and an 80 μm spot diameter. Depth profiles were recorded using the Qtegra (Thermo Scientific) software package. Monitored masses included ^{24}Mg, ^{27}Al, ^{44}Ca, ^{55}Mn, ^{88}Sr, ^{138}Ba and ^{238}U (Fig. 3). Calibration was performed against U.S. National Institute of Standards and Technology SRM 610 glass ablated at a higher energy density (approximately 5 J/cm^2) with ^{44}Ca as an internal standard using the values of Jochum et al. (2011) and assuming natural isotopic abundances. In addition, an in-house matrix-matched standard, based on an Iceland spar was ablated at lower energy density (1 J/cm^2) with

known Mg and Sr concentrations (Raitzsch et al., 2010) to check for the effect of changing energy densities. The constant elemental ratios in the ablation profiles with respect to depth indicate that post-depositional processes did not affect the shells and therefore the ^{87}Sr/^{86}Sr ratios are considered original.

3.3. Strontium isotope analyses

To determine ^{87}Sr/^{86}Sr ratios, 0.01-0.6 mg of ostracod(s) were dissolved in 0.5 ml acetic acid and centrifuged to separate the solution from any residues. No residues were observed. The so-

lution was then pipetted into a separate beaker and evaporated to dryness and then re-dissolved in concentrated HNO_3 (1 drop), evaporated to dryness and again dissolved in concentrated HNO_3 (2 drops) and evaporated to dryness. The samples were then dissolved in 0.5 ml 3N HNO_3 and stored on a hotplate for 1 h. Samples were put in an ultrasonic bath for 15 min before chromatographic separation. 0.4 ml of the samples was introduced to chromatographic columns composed of "Elchrom Sr spec" ion exchange resin to isolate the strontium fraction.

Strontium isotope analyses were carried out on a Finningan MAT 262 thermal ionisation mass spectrometer (TIMS) at the Vrije University (Amsterdam) running in the 'static' mode. Strontium isotope ratios were corrected for instrumental mass fractionation by normalizing to $^{86}Sr/^{88}Sr = 0.1194$. Samples were analyzed over a two-year period during which degradation of Faraday cup performance led to replacement of some of the Faraday cups and changes in the cup configurations used. Data are reported for three distinct analytical periods. Repeated measurements of the international standard NBS-987 yielded averages of respectively 0.710273 ± 0.000008 (2σ), n = 28; 0.710259 ± 0.000011 (2σ), n = 18; 0.710257 ± 0.000006 (2σ), n = 22. Data were normalized to the long term average value obtained for NBS 987 over the previous 5 years of 0.710254 ± 0.000005 (2σ), n > 100. The strontium blanks were <330 pg (average 197) and negligible relative to the overall amount of strontium analyzed from the ostracods (>100 ng).

3.4. Strontium isotope mass-balance models

The strontium isotope composition ($^{87}Sr/^{86}Sr$) of restricted water masses is determined by mixing of local sources such as hydrothermal vents and river water. These local inputs have their own typical isotopic composition and concentrations as a function of lithology in the catchment (Vonhof et al., 2003; Vasiliev et al., 2010). To comprehend the $^{87}Sr/^{86}Sr$ of the Paratethys during the MSC, a mass-balance model was applied based on modern isotopic inputs from the most important strontium sources for these basins:

$$^{87/86}Sr_{Paratethys}$$
$$= \frac{(F_a \cdot {}^{87/86}Sr_a) + (F_b \cdot {}^{87/86}Sr_b) \cdots + (F_z \cdot {}^{87/86}Sr_z)}{F_a + F_b \cdots + F_z}$$

wherein F_x is the strontium flux (mol/yr) and $^{87/86}Sr_x$ is the strontium isotope composition of a certain source.

The strontium flux is given by

$$F_x = Q_x \cdot C_x$$

wherein F_x is the strontium flux (mol/yr), Q_x is the discharge (L/yr) and C_x is the strontium concentration of the water (mol/L). Note that a certain increase in discharge does not imply a proportional increase of the strontium flux, because strontium concentrations are known to drop with increasing discharge rates (Palmer and Edmond, 1989).

Since the exact isotopic compositions and flux sizes are unknown for Messinian times, we used present-day values to predict the $^{87}Sr/^{86}Sr$ ratios of the Black and Caspian Seas waters during the MSC (Table 1). We consider this approach valid because the catchments of these rivers have not changed appreciably since the late Miocene (Popov et al., 2006).

3.5. Gypsum saturation calculations

In order to investigate the amount of evaporation necessary for gypsum formation ($CaSO_4 *2 H_2O$), calculations were performed

on modern Mediterranean and Caspian seawater using PHREEQC (Parkhurst and Appelo, 2013) at 25 °C with the Pitzer database. The chemical composition of the fluids used in the PHREEQC calculations are given in Table 2. The gypsum saturation level (Ω^*_{gypsum}) of seawater is calculated as follows:

$$\Omega^*_{gypsum} = \frac{IAP}{K_{sp}}$$

in which K_{sp} is the salinity-dependent solubility of gypsum at 25 °C (Sun et al., 2015) and IAP is the ion activity product of free dissolved calcium and sulfate, $\{Ca^{2+}\}\{SO_4^{2-}\}$. If $IAP > K_{sp}$, gypsum can precipitate from the oversaturated water. Average seawater composition (Broecker and Peng, 1982) was used for Mediterranean seawater calculation, modern Caspian seawater composition was taken from (Clauer et al., 2000) and modified Caspian seawater was obtained by removing sodium and chloride (potassium was retained and used to correct for charge imbalance). Standard evaporation (-H_2O) and mixing (MIX) options available in PHREEQC were used.

4. Results

4.1. Strontium isotopes

After a mechanical cleaning procedure, samples were first evaluated for potential diagenetic alteration. Samples with abundant ostracods were screened by obtaining a trace metal depth profile. Multiple trace elements were used as indicators of potential sources of contamination. Al and U are indicative of shell surface contamination by clay particles, Mn would signal secondary carbonate and/or manganese (hydr)oxides overgrowth. Although minor peaks in Al/Ca and U/Ca ratios indicated that there was still some contamination present on the outside of the ostracod shell despite the cleaning procedure (Fig. 3), the quantity of these 'contamination peaks' is low in comparison to the total quantity of the inner shell. For example, ^{88}Sr counts in the $^{24}Mg/^{44}Ca$ peak of AJ79 account only for <0.1% of the Sr content of the shell. The constant elemental ratios in the ablation profiles furthermore indicate that post-depositional processes such as recrystallization and/or solid-state diffusion did not affect $^{87}Sr/^{86}Sr$ and therefore none of the samples were considered appreciably affected by diagenetic alteration.

Our strontium isotope records from the Paratethys indicate three main hydrological phases in the late Miocene (Fig. 2; Table 3). Predating the MSC, $^{87}Sr/^{86}Sr$ ratios in the Paratethys are relatively low (0.70825) and close to the present-day Caspian Sea values (0.7082) (Clauer et al., 2000). At present, the Caspian Basin is isolated and its $^{87}Sr/^{86}Sr$ ratio is mainly determined by the Volga river and hydrothermal vents that supply relatively unradiogenic Sr (Clauer et al., 2000). The similarity in $^{87}Sr/^{86}Sr$ ratios with the present-day Caspian Sea indicates that the pre-MSC Paratethys Sea was disconnected from the ocean as well. At ~6.1 Ma, a rise in $^{87}Sr/^{86}Sr$ ratios is recorded, with the Caspian Sea data approaching open marine values (Fig. 2). The increase in $^{87}Sr/^{86}Sr$ ratios coincides with the regional Pontian Flood (Krijgsman et al., 2010; Grothe et al., 2014; Van Baak et al., 2017). This marine transgressive event connected the Black and Caspian Seas with the Mediterranean and some central European (Dacian and Pannonian) basins (Popov et al., 2006). Remarkably, marine ratios are not recorded in our Black Sea section, possibly because bottom water anoxia prevented the presence of ostracods during the 'peak-flooding'. Following this transgressive event, $^{87}Sr/^{86}Sr$-values of the Black and Caspian Seas decrease again and cluster around 0.7084-0.7085 throughout the MSC interval (Fig. 2). Although the Caspian Sea $^{87}Sr/^{86}Sr$ ratios are generally slightly lower (~0.7084), the similarity with the Black Sea values strongly supports a sustained

Table 2
Chemical composition of the fluids used in the PHREEQC calculations: Mediterranean Seawater (Med. SW; after Nordstrom et al., 1979), Caspian/Black Seawater (C/B SW, after Clauer et al., 2000 except for Dissolved Inorganic Carbon (DIC), which is from Meybeck, 1993), younger C/B SW (yC/B SW; without sodium chloride) and C/B SW and yC/B SW evaporated until equilibrium with gypsum was reached (with subscript evap).

	Med. SW	C/B SW	C/B SW$_{evap}$	yC/B SW	yC/B SW$_{evap}$
pH	8.2	7.0	6.9	7.0	7.0
Salinity	37	15	43	15	14
Ω_{gypsum}	0.20	0.33	1.00	0.33	1.00
Total concentrations (mmol/kgw)					
DIC	2.20	0.44	1.24	0.44	0.80
Total Ca	10.9	8.03	22.7	8.03	14.6
Total Cl	575	143	405	0	0
Total K	11.0	2.12	6.00	2.12	3.87
Total Mg	55.1	28.8	81.3	28.8	52.5
Total Na	494	131	369	0	0
Total SO$_4$	29.8	31.2	88.3	31.2	57.0
Ion (pair) activities (unitless)					
{HCO$_3^-$}	1.19E-03	2.72E-04	6.30E-04	2.73E-04	4.63E-04
{CO$_3^{2-}$}	9.01E-06	1.24E-07	2.20E-07	1.25E-07	1.92E-07
{Ca^{2+}}	2.47E-03	1.87E-03	4.16E-03	2.07E-03	3.06E-03
{Cl$^-$}	3.58E-01	9.95E-02	2.51E-01	0	0
{K$^+$}	7.16E-03	1.50E-03	3.84E-03	1.63E-03	2.84E-03
{Mg^{2+}}	1.37E-02	7.52E-03	1.73E-02	8.74E-03	1.31E-02
{MgCO$_3^0$}	1.05E-04	7.93E-07	3.23E-06	9.24E-07	2.13E-06
{MgOH$^+$}	3.47E-06	1.16E-07	2.02E-07	1.36E-07	1.84E-07
{Na$^+$}	3.49E-01	9.55E-02	2.55E-01	0	0
{SO$_4^{2-}$}	2.49E-03	5.25E-03	7.38E-03	7.26E-03	9.83E-03
Ion activity ratios					
{Ca^{2+}}/{Cl$^-$}	6.88E-03	1.88E-02	1.66E-02		
{SO$_4^{2-}$}/{Cl$^-$}	6.94E-03	5.28E-02	2.94E-02		

connection between these two basins. We have no data from the Black Sea between 5.6-5.3 Ma because of a stratigraphic hiatus in the section, but the stability of the Caspian Sea values, as well as biogeographic data, suggests that these basins remained connected (Vasiliev et al., 2013).

4.2. Mass balance model for the Paratethys Sea

The ^{87}Sr/^{86}Sr of the Paratethys seawater was calculated for four different input scenarios (Table 1):

(i) main rivers only (Danube, Dnieper Don, Volga);
(ii) main rivers and hydrothermal vents;
(iii) main rivers, hydrothermal vents and Mediterranean inflow;
(iv) main rivers and Mediterranean inflow.

We consider the clustering of ^{87}Sr/^{86}Sr ratios around 0.7084-0.7085 to represent a system in which the Black and Caspian Seas are 'fully connected'. Mass balance calculations for scenarios (i) and (ii), based on modern strontium input from the most important sources, however, yields a lower ^{87}Sr/^{86}Sr ratio: ~0.7083 and 0.7082, respectively. Therefore, a source of more radiogenic Sr would be required to explain our record. Since the late Miocene drainage system was very similar to present-day (Popov et al., 2006), the most likely additional source for high ^{87}Sr/^{86}Sr ratios is open marine water. To quantify how much inflow of marine waters is required to explain our measured strontium records, scenario (iii) and (iv) were evaluated. Adding an open marine source via a "Bosphorus"-like strait requires only ~4-10% of present-day marine input to explain the observed Sr isotope data for the Black and Caspian Seas (scenario iii). A further reduction of the present-day inflow down to 1-5% is enough to approach the measured ^{87}Sr/^{86}Sr ratios with scenario (iv) in the mass-balance. Such an inferred marine inflow into the Black Sea agrees with late Miocene proxy records showing presence of alkenones typical for marine conditions in the Black Sea (Vasiliev et al., 2013).

5. Discussion

5.1. Paratethys pacing of the MSC

Combining our new Black and Caspian Sea Sr isotope records with that of the Mediterranean, four main circulation modes can be identified between 6.7 and 5.0 Ma (Fig. 2).

Mode 1 (6.7-6.1 Ma): Before 6.1 Ma, ^{87}Sr/^{86}Sr ratios of the Black and Caspian Seas are the lowest. The similarity in ^{87}Sr/^{86}Sr ratios with the present-day isolated Caspian Sea (Fig. 2), coupled with our mass balance calculations, indicates that the two basins were disconnected from the open ocean forming a unified Paratethys Lake, which was dominantly filled by local rivers. Coeval ^{87}Sr/^{86}Sr values from the Mediterranean mostly plot on the ocean curve, attesting that the Mediterranean was a marine basin connected to the Atlantic.

Mode 2 (6.1-5.55 Ma): At ~6.1 Ma, a major transgressive event (i.e. the Pontian Flood after Krijgsman et al., 2010) connected the Paratethys to the Mediterranean. Despite the low resolution record, this short-lived event is reflected in the Paratethys Sr signal which shows a peak at 6.1 Ma, reaching values close to the marine curve (Fig. 2). The inflow of marine water into the fresh-brackish Paratethys lake may have created a two-way exchange at the gateway (cf. Marzocchi et al., 2016). The establishment of a Paratethyan flow towards the Mediterranean has recently been detected in the biomarker records of the Eastern Mediterranean that show a sudden freshening of the surface waters at ~6.1 Ma (Vasiliev et al., 2019).

The ^{87}Sr/^{86}Sr values of MSC Stage 1 and 2 evaporites are significantly offset from the oceanic curve (Fig. 2), indicating that large amounts of non-marine water spilled into the Mediterranean. It is not surprising that Mediterranean ^{87}Sr/^{86}Sr measured on the MSC Primary Lower Gypsum (Stage 1) remain close to oceanic values because the connection with the Atlantic Ocean, although restricted, was still rather efficient. The onset of the MSC at 5.97 Ma is often linked to the time that ^{87}Sr/^{86}Sr of Mediterranean

Table 3
Sample codes, stratigraphic position, regional stages, ages (in Ma) levels, ostracod species and $^{87}Sr/^{86}Sr$ ratios with 2σ error of all analysed samples.

| Sample	Stratigraphic level (m)	Parathys (sub)stages	Age (Ma)	Rough age estimate (Ma)	Ostracods and foraminifera species	$^{88}Sr/^{87}Sr$
TR23	-329.00	Upper Maeotian	6.2 - 8.2	7.75	*Cyprideis* (juveniles)	0.708084 ± 10
TH36	-298.00	Upper Maeotian	6.2 - 8.2	7.2	*Condon? neglecta*	0.708234 ± 9
TR27	-269.00	Upper Maeotian	6.2 - 8.2	6.7	*Ammonia beccom*	0.708228 ± 10
TR30	-266.00	Upper Maeotian	6.2 - 8.2	6.6	*Cyprideis* sp.	0.708229 ± 8
TR41	-255.00	Upper Maeotian	6.2 - 8.2Ma	6.55	*Ammonia beccom* + *Cyprideus* sp. (juvenile)	0.708286 ± 8
TR71	-206.00	Upper Maeotian	6.160	–	*Cyprideis* sp.	0.708284 ± 16
TR80	-197.00	Pontian Foram interval	6.100	–	*Cyprideis, Leptocyther sulakensis*	0.708234 ± 7
TR80	-197.00	Pontian Foram interval	6.100	–	*Cyprideis* sp.	0.708231 ± 10
TR82	-195.00	Pontian Foram interval	6.090	–	*Cyprideis*	0.708265 ± 8
TR83-c	-194.00	Pontian Foram interval	6.088	–	*Cyprideis* sp.	0.708220 ± 9
TR89	-185.00	Pontian	6.050	–	*Pontoniella lotzyr*	0.708397 ± 9
TR89a	-185.00	Pontian	6.050	–	*Amnicythere* sp.	0.708433 ± 10
TR92	-182.00	Pontian	6.040	–	*Cyprideis* sp.	0.708400 ± 9
TR101	-173.00	Pontian	6.000	–	*Caspiocypris atta*	0.708404 ± 10
TR109	-165.00	Pontian	5.960	–	*Caspiocypris atta*	0.708415 ± 9
TR115	-148.00	Pontian	5.900	–	*Caspiocypris atta*	0.708503 ± 16
TR117	-146.00	Pontian	5.870	–	*Caspiocypris atta*	0.708474 ± 9
TR126	-133.00	Pontian	5.840	–	*Caspiocypris atta*	0.708531 ± 9
TK38	-117.00	Pontian	5.750	–	*Caspiocypris atta*	0.708505 ± 9
TK24	-107.00	Pontian	5.670	–	*Caspiocypris atta*	0.708567 ± 9
TK18	-101.00	Pontian	5.630	–	*Caspiocypris atta*	0.708538 ± 9
TK12	-96.00	Pontian	5.620	–	*Caspiocypris atta*	0.708520 ± 9
TK09	-94.00	Pontian	5.610	–	*Caspiocypris? atta*	0.708608 ± 9
TK52	-77.00	Kimmerian	5.100	–	*Casprocypiris* (fragments)	0.708434 ± 9
AA18	5.60	Upper Maeotian	6.125	–	*Leptocythere sulakensis*	0.708297 ± 8
AA22	7.00	Pont: Foram interval	6.110	–	*Leptocythere sulakensis*	0.708729 ± 10
AA24	7.58	Pont: Foram interval	6.080	–	*Leptocythere sulakensis*	0.708331 ± 9
AA114	33.60	Pontian	5.930	–	*Amnicythere palimpsesta*	0.708360 ± 9
AA134	39.80	Pontian	5.870	–	*Amnicythere palimpsesta*	0.708406 ± 12
AA146	42.90	Pontian	5.850	–	*Amnicythere palimpsesta, Caspiocypris*	0.708277 ± 10
AA150	43.95	Pontian	5.840	–	*Amnicythere palimpsesta*	0.708277 ± 9
AA180	51.75	Pontian	5.790	–	*Amnicythere palimpsesta*	0.708422 ± 8
AA200	57.00	Pontian	5.760	–	*Amnicythere palimpsesta*	0.708423 ± 9
AJ09	59.00	Pontian	5.750	–	*Amnicythere palimpsesta*	0.708488 ± 9
AJ19	61.50	Pontian	5.740	–	*Amnicythere palimpsesta*	0.708524 ± 9
AA215	61.55	Pontian	5.740	–	*Amnicythere palimpsesta*	0.708494 ± 9
AJ26	64.00	Pontian	5.730	–	*Amnicythere palimpsesta*	0.708457 ± 9
AJ79	76.75	Pontian	5.630	–	*Amnicythere palimpsesta*	0.708485 ± 9
AJ111	84.75	Pontian	5.590	–	*Amnicythere palimpsesta*	0.708442 ± 9
AJ123	87.75	Pontian	5.580	–	*Amnicythere palimpsesta*	0.708435 ± 13
AJ142	92.50	Pontian	5.550	–	*Amnicythere palimpsesta*	0.708402 ± 9
AJ204	113.50	Pontian	5.450	–	*Amnicythere palimpsesta*	0.708433 ± 7
AJ217	119.75	Pontian	5.420	–	*Amnicythere palimpsesta*	0.708456 ± 8
AJ223	122.00	Pontian	5.410	–	*Amnicythere palimpsesta*	0.708452 ± 10
AJ234	127.75	Pontian	5.380	–	*Amnicythere palimpsesta*	0.708473 ± 9

seawater starts to deviate from open ocean Sr-isotope values, but $^{87}Sr/^{86}Sr$ of foraminifers just preceding the onset of the MSC already show an offset (Fig. 2; Roveri et al., 2014b). Strontium isotope data from individual gypsum beds of the Northern Apennines show that gypsum precipitation started from a seawater body marked by non-marine contributions and that the influence of marine input increased through time within a precessional cycle (Reghizzi et al., 2018). These Sr-isotope values are so far ascribed to variations in freshwater discharge from the major peri-Mediterranean rivers only (e.g. Rhône and Nile) (García-Veigas et al., 2018; Reghizzi et al., 2018). We postulate here that Paratethys may have contributed to the freshening of the Mediterranean surface waters during PLG formation. The westward spread of brackish Paratethyan waters could have been facilitated by the density contrast with the saline marine Mediterranean, which prevents mixing and favors a strongly stratified water column (cf. the MSC scenario of García-Veigas et al., 2018). The absence of both Paratethyan and Atlantic faunal assemblages in MSC Stage 1 and 2 deposits suggests that an ecological barrier (probably salinity) was present that prevented faunal exchange with the Mediterranean during this time.

Mode 3 (5.55-5.33): The low $^{87}Sr/^{86}Sr$ values of MSC Stage 3 (0.7085-0.7087) imply a major contribution from Paratethyan wa-

ters into the Mediterranean, at least within the surface layer, and a further reduction of Atlantic inflow (Fig. 2). To approach the $^{87}Sr/^{86}Sr$ values that characterize Stage 3, the present-day inflow of the Atlantic needs to be reduced by at least a factor of 1000. With a strongly reduced Atlantic inflow, a volume of Paratethys Sea inflow similar to present-day Black Sea inflow is sufficient to approach the observed Mediterranean $^{87}Sr/^{86}Sr$. A strongly reduced Atlantic inflow, however, would lead to a drop in Mediterranean water levels, which is in line with the classic desiccation model (Hsü et al., 1973), but not with the idea that the Mediterranean remained water-filled (Roveri et al., 2014a; Stoica et al., 2016). Reduced mixing between a low salinity surface water layer and deeper highly saline Atlantic waters provides an alternative mechanism (Marzocchi et al., 2016; García-Veigas et al., 2018). The high density of the brine responsible for halite precipitation (MSC Stage 2) may have prevented waters from the Paratethys to mix due to the large density contrast. Consequently, reduced mixing of these low salinity Paratethyan waters would facilitate the spread of these waters as a thin but extensive low salinity lid across the entire Mediterranean. Environmental conditions in the Mediterranean during Upper Gypsum deposition (MSC substage 3.1) were still unfavorable for most Paratethyan fauna to migrate westward.
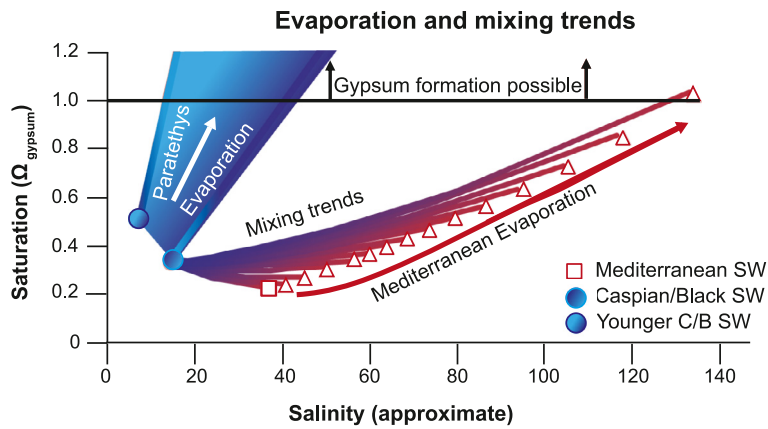
Fig. 4. Model results for evaporation of Mediterranean and Caspian seawater during the MSC. Square is for average seawater (SW) and triangles for progressive evaporation of this SW; light circle is for modern Caspian SW (Clauer et al., 2000) and light diamonds for progressive evaporation of this water; dark circle is for modified Caspian SW (sodium chloride free, i.e., NaCl-free) and light diamonds for progressive evaporation of modified Caspian SW; the horizontal solid line indicates equilibrium with gypsum and above this line, gypsum precipitation is thermodynamically possible; other solid lines relate to mixing of (evaporated) Mediterranean SW and modern Caspian SW.

A marked hydrological change took place in the Mediterranean at 5.42 Ma and the onset of the Lago-mare (MSC substage 3.2; Roveri et al., 2014a), when numerous Paratethyan ostracod and mollusk species invaded the Mediterranean (Gliozzi et al., 2007; Stoica et al., 2016). It must be noted here that also during substage 3.2 some gypsum layers formed in the Mediterranean (e.g., Eraclea Minoa; Roveri et al., 2014a). The density contrast between Mediterranean and Paratethyan waters may have triggered a huge outflow pump (Marzocchi et al., 2016) that can explain the existence of Black Sea endemic fauna in even the westernmost Mediterranean basins during MSC Stage 3.2 (Guerra-Merchán et al., 2010; Stoica et al., 2016).

Increased input from the Nile River or other major peri-Mediterranean rivers might have added to the observed isotopic ratios (Gladstone et al., 2007), but evidence exists for inflow from the Black Sea in the form of typical Paratethys fauna (Gliozzi et al., 2007; Stoica et al., 2016). We postulate here that inflow from the Paratethys forms an alternative and simpler scenario to explain the low $^{87}Sr/^{86}Sr$ values of Stage 3. The extensive hinterland draining into the Black and Caspian Sea (Fig. 1) delivers water roughly one order of magnitude higher in Sr concentrations compared to Nile river water. Hence, although the Nile might also have added low radiogenic strontium, the observed temporal changes in $^{87}Sr/^{86}Sr$ are alternatively explained by a Paratethys source. Drainage from other North African basins (including Lake Chad) would have, in contrast to the Nile, increased the $^{87}Sr/^{86}Sr$ ratios of the Mediterranean because their catchments lack extensive Rb-depleted basaltic rocks with a characteristic low $^{87}Sr/^{86}Sr$ (Topper et al., 2014).

Mode 4 (5.33-5.0 Ma): Finally, during the onset of the Pliocene, the Atlantic-Mediterranean connection is restored and marine conditions return in the Mediterranean. Paratethys most likely continued to drain low salinity water into the Mediterranean, but this is no longer detected in the strontium isotope values. The restored connection to the Atlantic Ocean converted Mediterranean $^{87}Sr/^{86}Sr$ ratios towards oceanic values, because ocean water has a 7-8 times higher Sr concentration than non-marine sources.

5.2. A brackish water trigger for gypsum formation during the MSC?

The new strontium isotope data strongly suggest the existence of a sustained connection between the Mediterranean and Paratethys during the entire MSC. This connection would have affected the Mediterranean water budget by adding low salinity water. While restriction of the Mediterranean-Atlantic gateway(s) is considered the principal criterion in explaining the formation of evaporites (Garcia-Castellanos and Villaseñor, 2011; Flecker et al.,

2015; Krijgsman et al., 2018), our data suggest that the onset of a Mediterranean-Paratethys connection, which preceded the first gypsum beds, somehow played a major role in shaping the MSC-events.

The gypsum deposits of MSC Stage 1 are all from shallow-water settings (<200 m) and contain low-salinity fluid inclusions with stable oxygen isotope signals indicative of large inputs of Na^+ and Cl^--depleted waters during their formation (Natalicchio et al., 2014; Evans et al., 2015). Natalicchio et al. (2014) proposed that local rivers enriched in Ca^{2+} and SO_4^{2-}, derived from partial dissolution and recycling of coeval marginal marine deposits, are the main source of non-marine Ca^{2+} and SO_4^{2-}. We here propose Paratethys may have contributed in three ways: 1) Freshwater from the Paratethys entering the strongly restricted Mediterranean Basin would certainly enhance stratification, resulting in a low-salinity surface-water layer that could influence the water composition in the individual shallow basins where MSC Stage 1 gypsum accumulated; 2) the freshwater surface-water from the Paratethys had relatively high concentrations of Ca^{2+} and SO_4^{2-} (cf. Clauer et al., 2000), and may have added Ca^{2+} and SO_4^{2-} to the underlying sea-water layer resulting in gypsum precipitating from a marine layer; 3) the low-salinity water with relatively high concentrations of Ca^{2+} and SO_4^{2-} itself provided the non-marine setting in which gypsum could precipitate by evaporation.

Interestingly, the Paratethyan waters flowing in to the Mediterranean are as high in calcium and sulfate as average seawater (cf. Clauer et al., 2000). At the same time, Paratethyan water has much lower sodium and chloride concentrations than average seawater (Table 2). These ions play a crucial role in gypsum formation, by affecting the ion activity product (IAP, $\{Ca^{2+}\}\{SO_4^{2-}\}$; see section 3.4). Dissolved sodium and chloride pair with sulfate and calcium in solution, respectively, thereby lowering the IAP and the saturation state (Ω^*_{gypsum}). In other words, high chloride and sodium concentrations, as found in seawater and evaporated seawater, increase gypsum solubility, and make it harder to reach super-saturated conditions in which gypsum can precipitate.

The impact of sodium and chloride concentrations on saturation state is clear: while average seawater and Caspian water have similar total calcium and sulfate concentrations, seawater is more strongly undersaturated (Fig. 4; Table 2). Moreover, to reach gypsum saturation normal seawater has to be concentrated by evaporation to a salinity of ~120. In contrast, evaporation of modern Caspian water becomes gypsum saturated at a salinity of ~40 (Fig. 4). Mixing Mediterranean Sea-water, or any of the solutions along its evaporation trend, with modern Caspian water enhances saturation but not enough for gypsum precipitation.
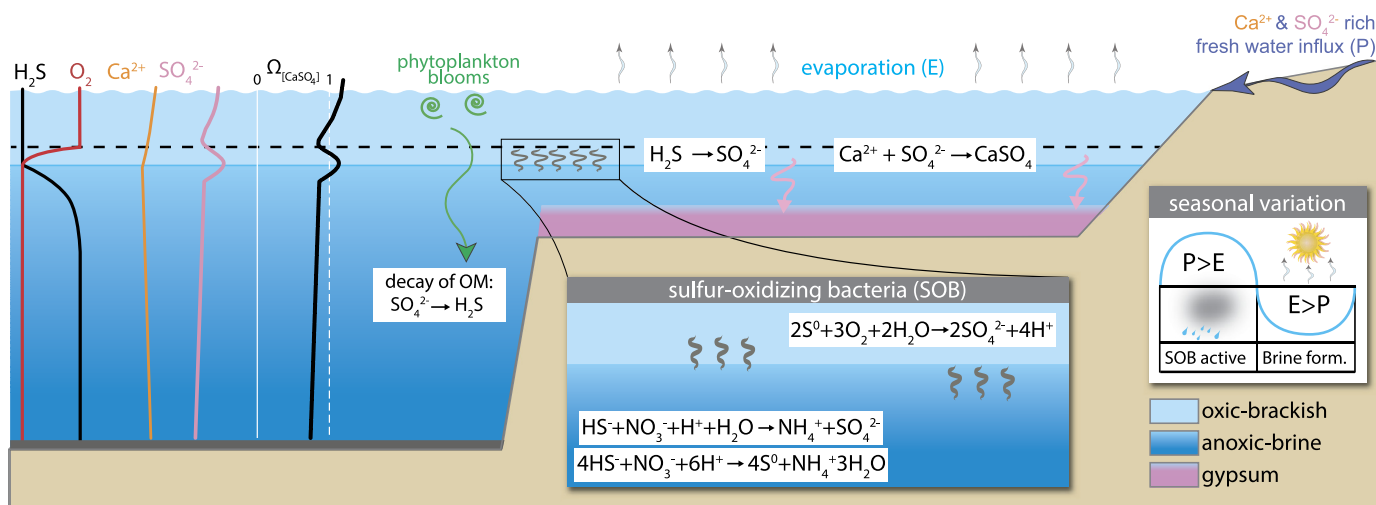
Fig. 5. Conceptual model illustrating the suggested role of sulfur-oxidizing bacteria (SOB) in biogeochemically meditated gypsum formation. SOB inhabiting a niche on the pycnocline profit from the availability of sulfide and oxygen. SOB transform reduced sulfur species (H_2S, S_0) into sulfate (SO_4^{2-}) and thereby raise the production of [Ca^{2+}] and [SO_4^{2-}], which may trigger gypsum precipitation. The nutrients in the upper part of the water-column promote productivity. Subsequent decay of this organic material in anoxic waters produces sulfides (H_2S), which are required to sustain the SOB-activity.

Miocene Paratethyan waters may even have had lower sodium and chloride contents than present-day Caspian water, because Paratethys was not the closed evaporative basin as the Caspian has been over the last ± 3 Ma (Palcu et al., 2019). High concentrations of sodium and chloride in sea water are the result of billions of years of weathering and the long residence times of these elements and consequently young waters are relatively impoverished in both elements. Assuming calcium and sulfate concentrations similar to modern Caspian water and negligible sodium and chloride, then evaporation of Paratethyan water leads to gypsum saturation at a salinity of ± 14 (Fig. 4). If the Paratethys water was lower in calcium and sulfate then assumed here, the saturation state would be lower (Ω^*_{gypsum} would be smaller), but the evaporation trend would be as steep as plotted in Fig. 4, leading to a similarly low salinity for gypsum saturation. The product of $\{Ca^{2+}\}\{SO_4^{2-}\}$ can also rise due to an increased influx of calcium and/or sulfate. Two superimposed water layers, both enriched in sulfate and calcium, can exchange ions by diffusion and influence the gypsum solubility product without increasing the overall salinity (Fig. 5). Additional sulfate can be provided by abiotic (e.g. Lin et al., 2016) or biologic (e.g. Bailey et al., 2009) oxidation of reduced sulfur compounds. The MSC gypsum and shale deposits contain ubiquitous large filamentous microfossils, interpreted initially as remains of algae (Vai and Ricci Lucchi, 1977), faecal pellets (Guido et al., 2007) or cyanobacteria (Panieri et al., 2010). More recently they have been interpreted as remains of sulfide-oxidizing bacteria (SOB), based on the identification of sulfur-containing minerals possibly derived from the diagenetic transformation of elemental sulfur stored within cytoplasm (Dela Pierre et al., 2014, 2015; Andreetto et al., 2019). SOBs do not provide useful paleobathymetrical and salinity information, but they play a key role in the biogeochemical sulfur cycle by producing SO_4^{2-} from the oxidation of reduced sulfur species [e.g. H_2S, S^{2-}] (e.g. Bailey et al., 2009). The exact role of microbes in gypsum precipitation is still poorly understood, but potential additional sulfate input from SOB would result in super saturation being reached at lower levels of evaporation than shown in Fig. 4 and hence potential gypsum formation at even lower salinities (Fig. 5).

5.3. Paratethys contribution to other gypsum deposits

Our observations suggest that shallow-basin MSC gypsum layers can be formed by evaporation of a low salinity water layer, partly sourced from the Paratethys Sea. Gypsum formation being influenced by Paratethyan water was probably not restricted to the Mediterranean MSC as numerous gypsum deposits are known from several former Paratethyan basins. Archetypes are the evaporites of the Badenian Salinity Crisis (13.8-13.4 Ma; Peryt, 2006; De Leeuw et al., 2010) of the Central Paratethys (Carpathian Foredeep, Transylvanian Basin, Pannonian Basin), and several other gypsum units have been described from the early and middle Miocene Paratethyan basins as well (see De Leeuw et al., 2018 and references therein). The paleogeographic configuration of the Badenian and Messinian Salinity Crises are very similar, with the evaporite basins in intermediate position between the open ocean and the restricted brackish water domain of the Eastern Paratethys (Palcu et al., 2017). More detailed geochemical studies of the Badenian and Messinian evaporites are needed to better understand the role of Eastern Paratethys waters, and the potential involvement of SOB on gypsum formation.

5.4. Pitfalls and future perspectives

All data so far indicate that Paratethys-Mediterranean connectivity existed during the latest Messinian and that Paratethyan water, with much higher concentrations of strontium, calcium and sulfate than river water, contributed as an additional low salinity water source to the Mediterranean hydrological balance during the different MSC stages. The remaining key question is now: How significant was the late Messinian Paratethys flux of low salinity water for the Mediterranean? And should the various hydrological, strontium, gypsum and climate models of the MSC be updated and revised? At this moment, no quantitative amounts of Paratethyan water fluxes are available for MSC times. In addition, the chemical composition of the Messinian Paratethys is still unknown; in this paper we have used the present-day Caspian values as the most likely modern analogue. More detailed studies on the paleoenvironmental and paleohydrological changes that occurred in Paratethys during the Messinian (Pontian stage in regional terminology) are therefore very welcome.

Despite the uncertainties in the exact location of the gateway(s) (see Van Baak et al., 2016), Mediterranean-Paratethys connectivity most likely has taken place via the Aegean domain (Fig. 1), an area with poorly dated Miocene successions that is generally considered as an intermediate domain, showing aspects of both Mediterranean and Paratethyan fauna (Popov et al., 2006).

Paratethyan fauna is absent in the Mediterranean during MSC Stage 1 and 2, sporadically occurring in MSC substage 3.1 (Eraclea Minoa, Sicily; Grossi et al., 2015), but omnipresent in substage 3.2. This trend may indicate an increase through time of the relative contribution of Paratethyan waters to the Mediterranean and/or a progressive change in Mediterranean salinity, which is the one of the main environmental factor that controls the proliferation of brackish Paratethyan organisms during the MSC. This salinity change is most likely amplified by the significant decrease, or even complete termination, of the Atlantic influx through the Gibraltar Corridor during Stage 3 (see Krijgsman et al., 2018 for details). Revised hydrological and climate models are thus necessary to test for different Atlantic-river-Paratethys influx values on Mediterranean strontium ratios and gypsum precipitation models. This will eventually also solve the question to what stage(s) the Paratethys has influenced the Mediterranean MSC.

6. Conclusions

Strontium isotope records from the Paratethys reveal several hydrological changes in the latest Miocene. Predating the MSC (>6.1 Ma), $^{87}Sr/^{86}Sr$ ratios are relatively low (0.70825), indicating that the Paratethys was mainly disconnected from the Mediterranean. At 6.1 Ma, a sudden rise in $^{87}Sr/^{86}Sr$ (max. 0.7087) corresponds to the Pontian Flood and reflects the initiation of Paratethys-Mediterranean connectivity. Throughout the MSC interval (5.97-5.33 Ma), $^{87}Sr/^{86}Sr$ ratios in Paratethys cluster around 0.7084-0.7085, values that are best explained by a severely reduced connection with $<10\%$ of the present-day inflow through the Bosphorus Strait.

The strontium isotope variations of Paratethys suggest a direct pacing of Mediterranean hydrology and MSC gypsum formation. The Mediterranean $^{87}Sr/^{86}Sr$ record shows a deviation from the open ocean curve at 6.1 Ma, when a connection with the Paratethys is established (Fig. 2). During MSC Stage 3 the Mediterranean $^{87}Sr/^{86}Sr$ values (down to ~ 0.7085) appear dominated by Paratethys waters, combined with a strongly reduced contribution of the Atlantic.

We propose that the high-density brine formation during the Mediterranean MSC may have prevented mixing of Paratethys waters forming an extensive low-salinity surface layer rich in calcium and sulfate. We show that evaporation of such a surface layer results in saturation with respect to gypsum at a salinity of ~ 40. This is in good agreement with recent salinity reconstructions of MSC gypsum based on fluid inclusions (Natalicchio et al., 2014; Evans et al., 2015).

This proposed mechanistic link between gypsum formation and low-saline water inputs from the Black Sea implies that climatic phenomena and evaporation rates in the Paratethys region, and the Atlantic Ocean, should be considered as additional potential drivers for the cyclic gypsum beds and low $^{87}Sr/^{86}Sr$ ratios of the Mediterranean MSC rather than African monsoon driven input from the Nile only. Our scenario provides new constraints for future quantitative models, that should include a supplementary Paratethys component in the Mediterranean hydrological balance and assess the proportion of riverine and Paratethys $^{87}Sr/^{86}Sr$ to lower the $^{87}Sr/^{86}Sr$ of the MSC Mediterranean water mass during gypsum precipitation.

Author contributions

AG, GJR, CvB, IV, FS, WK all contributed to the conceptualization of the research. AG, CvB, IV, MS, WK sampled the sections, MS, FS were in charge of the faunal analyses, AG, GJR, GD performed and analyzed the strontium measurements, GJR, MW, JJM performed and analyzed the geochemical models, AG, GJR, FS, WK prepared the original draft, FA, MW, GJR, IV, GD and WK took care of the revisions and editing of the final manuscript.

Declaration of competing interest

The authors declare that they have no known competing financial interests or personal relationships that could have appeared to influence the work reported in this paper.

References

Andreetto, F., Dela Pierre, F., Gibert, L.B., Natalicchio, M., Ferrando, S., 2019. Potential fossilized sulfide-oxidizing bacteria in the upper Miocene sulfur-bearing limestones from the Lorca Basin (SE Spain): paleoenvironmental implications. Front. Microbiol. 10, 1031. https://doi.org/10.3389/fmicb.2019.01031.

Bailey, J.V., Orphan, V.J., Joye, S.B., Corsetti, F.A., 2009. Chemotrophic microbial mats and their potential for preservation in the rock record. Astrobiology 9, 843–859. https://doi.org/10.1089/ast.2008.0314.

Brass, G.W., 1976. The variation of the marine ratio during Phanerozonic time: interpretation using a flux model. Geochim. Cosmochim. Acta 40, 721–730.

Broecker, W., Peng, T., 1982. Tracers in the Sea. Lamont-Doherty Geol. Obs., Palisades, NY. 690.

Bryden, H.L., Candela, J., Kinder, T.H., 1994. Exchange through the Strait of Gibraltar. Prog. Oceanogr. 33, 201–248.

Clauer, N., Chaudhuri, S., Toulkeridis, T., Blanc, G., 2000. Fluctuations of Caspian Sea level: beyond climatic variations? Geology 28, 1015–1018.

Costanzo, A., Cipriani, M., Feely, M., Cianfione, G., Dominici, R., 2019. Messinian twinned selenite from the Catanzaro Trough, Calabria, Southern Italy: field, petrographic and fluid inclusion perspectives. Carbonates and Evaporites 34, 743–756. https://doi.org/10.1007/s13146-019-00516-0.

De Lange, G.J., Krijgsman, W., 2010. Messinian salinity crisis: a novel unifying shallow gypsum/deep dolomite formation mechanism. Mar. Geol. 275, 273–277. https://doi.org/10.1016/j.margeo.2010.05.003.

De Leeuw, A., Bukowski, K., Krijgsman, W., Kuiper, K.F., 2010. Age of the Badenian salinity crisis; impact of Miocene climate variability on the circum-Mediterranean region. Geology 38 (8), 715–718.

De Leeuw, A., Tulbure, M., Kuiper, K.F., Melinte-Dobrinescu, M.C., Stoica, M., Krijgsman, W., 2018. New 39Ar/40Ar, magnetostratigraphic and biostratigraphic constraints on the termination of the Badenian Salinity Crisis: indications for tectonic improvement of basin interconnectivity in Southern Europe. Glob. Planet. Change 169, 1–15. https://doi.org/10.1016/j.gloplacha.2018.07.001.

Dela Pierre, F., Clari, P., Natalicchio, M., Ferrando, S., Giustetto, R., Lozar, F., Lugli, S., Manzi, V., Roveri, M., Violanti, D., 2014. Flocculent layers and bacterial mats in the mudstone interbeds of the Primary Lower Gypsum unit (Tertiary Piedmont basin, NW Italy): archives of palaeoenvironmental changes during the Messinian salinity crisis. Mar. Geol. 355, 71–87.

Dela Pierre, F., Natalicchio, M., Ferrando, S., Giustetto, R., Birgel, D., Carnevale, G., Gier, S., Lozar, F., Marabello, D., Peckmann, J., 2015. Are the large filamentous microfossils preserved in Messinian gypsum colorless sulfide-oxidizing bacteria? Geology 43, 855–858.

Evans, N.P., Turchyn, A.V., Gázquez, F., Bontognali, R.R., Chapman, H.J., Hodell, D.A., 2015. Coupled measurements of δ18O and δD of hydration water and salinity of fluid inclusions in gypsum from the Messinian Yesares Member, Sorbas Basin (SE Spain). Earth Planet. Sci. Lett. 430, 499–510.

Flecker, R., Ellam, R.M., 2006. Identifying Late Miocene episodes of connection and isolation in the Mediterranean–Paratethyan realm using Sr isotopes. Sediment. Geol. 188–189, 189–203. https://doi.org/10.1016/j.sedgeo.2006.03.005.

Flecker, R., Krijgsman, W., Capella, W., de Castro Martíns, C., Dmitrieva, E., Mayser, J.P., Marzocchi, A., Modestu, S., Ochoa, D., Simon, D., Tulbure, M., van den Berg, B., van der Schee, M., de Lange, G., Ellam, R., Govers, R., Gutjahr, M., Hilgen, F., Kouwenhoven, T., Lofi, J., Meijer, P., Sierro, F.J., Bachiri, N., Barhoun, N., Alami, A.C., Chacon, B., Flores, J.A., Gregory, J., Howard, J., Lunt, D., Ochoa, M., Pancost, R., Vincent, S., Yousfi, M.Z., 2015. Evolution of the Late Miocene Mediterranean-Atlantic gateways and their impact on regional and global environmental change. Earth-Sci. Rev. 150, 365–392. https://doi.org/10.1016/j.earscirev.2015.08.007.

Garcia-Castellanos, D., Villaseñor, A., 2011. Messinian salinity crisis regulated by competing tectonics and erosion at the Gibraltar arc. Nature 480, 359–363.

García-Veigas, J., Cendon, D.L., Gibert, L., Lowenstein, T.K., Artiaga, D., 2018. Geochemical indicators in Western Mediterranean Messinian evaporites: implications for the salinity crisis. Mar. Geol. 403, 197–214. https://doi.org/10.1016/j.margeo.2018.06.005.

Gerstenberger, H., Haase, G., El Nour, F.A., 1997. The origin of strontium and the strontium isotope budget of the river Nile. Isot. Environ. 33, 349–356.

Gillet, H., Lericolais, G., Réhault, J.-P., 2007. Messinian event in the Black Sea: evidence of a Messinian erosional surface. Mar. Geol. 244, 142–165. https://doi.org/10.1016/j.margeo.2007.06.004.

Gladstone, R., Flecker, R., Valdes, P., Lunt, D., Markwick, P., 2007. The Mediterranean hydrologic budget from a Late Miocene global climate simulation. Palaeogeogr. Palaeoclimatol. Palaeoecol. 251, 254–267. https://doi.org/10.1016/j.palaeo.2007.03.050.

Gliozzi, E., Ceci, M.E., Grossi, F., Ligios, S., 2007. Paratethyan Ostracod immigrants in Italy during the Late Miocene. Geobios 40, 325–337. https://doi.org/10.1016/j.geobios.2006.10.004.

Grossi, F., Gliozzi, E., Anadón, P., Castorina, F., Voltaggio, M., 2015. Is Cyprideis agrigentina Decima a good paleosalinometer for the Messinian Salinity Crisis? Morphometrical and geochemical analyses from the Eraclea Minoa section (Sicily). Palaeogeogr. Palaeoclimatol. Palaeoecol. 419, 75–89.

Grothe, A., Sangiorgi, F., Mulders, Y.R., Vasiliev, I., Reichart, G.-J., Brinkhuis, H., Stoica, M., Krijgsman, W., 2014. Black sea desiccation during the Messinian Salinity Crisis: fact or fiction? Geology 42. https://doi.org/10.1130/G35503.1.

Guerra-Merchán, A., Serrano, F., Garcés, M., Gofas, S., Esu, D., Gliozzi, E., Grossi, F., 2010. Messinian Lago-Mare deposits near the Strait of Gibraltar (Malaga Basin, S Spain). Palaeogeogr. Palaeoclimatol. Palaeoecol. 285, 264–276. https://doi.org/10.1016/j.palaeo.2009.11.019.

Guido, A., Jacob, J., Gautret, P., Laggoun-Defarge, F., Mastandrea, A., Russo, F., 2007. Molecular fossils and other organic markers as palaeoenvironmental indicators of the Messinian Calcare di Base Formation: normal versus stressed marine deposition (Rossano Basin, northern Calabria, Italy). Palaeogeogr. Palaeoclimatol. Palaeoecol. 255, 265–283. https://doi.org/10.1016/j.palaeo.2007.07.015.

Hsü, K., Ryan, W.B.F., Cita, M., 1973. Late Miocene desiccation of the Mediterranean. Nature 242, 240–244.

Hsü, K.J., Giovanoli, F., 1980. Messinian event in the Black Sea. Palaeogeogr. Palaeoclimatol. Palaeoecol. 29, 75–93.

Jarosz, E., Teague, W.J., Book, J.W., Beşiktepe, Ş.T., 2013. Observed volume fluxes and mixing in the Dardanelles strait. J. Geophys. Res., Oceans 118, 5007–5021.

Jochum, K.P., Weis, U., Stoll, B., Kuzmin, D., Yang, Q., Raczek, I., Dorrit, E.J., Stracke, A., Birbaum, K., Frick, D.A., Guenther, D., Enzweiler, J., 2011. Determination of reference values for NIST SRM 610-617 glasses following ISO guidelines. Geostand. Geoanal. Res. 35, 397–429.

Krijgsman, W., Capella, W., Simon, D., Hilgen, F.J., Kouwenhoven, T.J., Th, P., Sierro, F.J., Tulbure, M.A., Van Den Berg, B.C.J., Van Der Schee, M., Flecker, R., 2018. The Gibraltar Corridor: watergate of the Messinian Salinity Crisis. Mar. Geol. 403, 238–246. https://doi.org/10.1016/j.margeo.2018.06.008.

Krijgsman, W., Fortuin, A.R., Hilgen, F.J., Sierro, F.J., 2001. Astrochronology for the Messinian Sorbas basin (SE Spain) and orbital (precessional) forcing for evaporite cyclicity. Sediment. Geol. 140, 43–60. https://doi.org/10.1016/S0037-0738(00)00171-8.

Krijgsman, W., Stoica, M., Vasiliev, I., Popov, V.V., 2010. Rise and fall of the Paratethys Sea during the Messinian Salinity Crisis. Earth Planet. Sci. Lett. 290, 183–191. https://doi.org/10.1016/j.epsl.2009.12.020.

Kroonenberg, S.B., et al., 2011. Two deltas, two basins, one river, one sea: the modern Volga Delta as an analogue of the Neogene productive series, South Caspian Basin. In: River Deltas - Concepts, Models and Examples, pp. 231–256.

Lin, Q., Wang, J., Algeo, T.J., Su, P., Hu, G., 2016. Formation mechanism of authigenic gypsum in marine methane hydrate settings: evidence from the northern South China Sea. Deep-Sea Res., Part 1, Oceanogr. Res. Pap. 115, 210–220. https://doi.org/10.1016/j.dsr.2016.06.010.

Lugli, S., Manzi, V., Roveri, M., Schreiber, B.C., 2010. The primary lower gypsum in the Mediterranean: a new facies interpretation for the first stage of the Messinian salinity crisis. Palaeogeogr. Palaeoclimatol. Palaeoecol. 297, 83–99. https://doi.org/10.1016/j.palaeo.2010.07.017.

Marzocchi, A., Flecker, R., van Baak, C.G.C., Lunt, D.J., Krijgsman, W., 2016. Mediterranean outflow pump: an alternative mechanism for the Lago-mare and the end of the Messinian Salinity Crisis. Geology 44. https://doi.org/10.1130/G37646.1.

Mason, P.R.D., Kraan, W.J., 2002. Attenuation of spectral interferences during laser ablation inductively coupled plasma mass spectrometry (LA-ICP-MS) using an rf only collision and reaction cell. J. Anal. At. Spectrom. 17, 858–867.

Meybeck, M., 1993. In: Wollast, Mackenzie, Chou (Eds.), Interactions of C, N, P and S Biogeochemical Cycles and Global Change. Springer-Verlag. Ch. 6.

Natalicchio, M., Dela Pierre, F., Lugli, S., Lowenstein, T.K., Feiner, S.J., Ferrando, S., Manzi, V., Roveri, M., Clari, P., 2014. Did Late Miocene (Messinian) gypsum precipitate from evaporated marine brines? Insights from the Piedmont Basin (Italy). Geology 42, 179–182.

Nordstrom, D.K., Plummer, L.N., Wigley, T.M.L., Wolery, T.J., Ball, J.W., Jenne, E.A., Bassett, R.L., Crerar, D.A., Florence, T.M., Fritz, B., Hoffman, M., Holdren Jr., G.R., Lafon, G.M., Mattigod, S.V., McDuff, R.E., Morel, F., Reddy, M.M., Sposito, G., Thrailkill, J., 1979. A comparison of computerized chemical models for equilibrium calculations in aqueous systems. In: Jenne, E.A. (Ed.), Chemical Modeling in Aqueous Systems, Speciation, Sorption, Solubility, and Kinetics, vol. 93. American Chemical Society, pp. 857–892.

Palcu, D.V., Golovina, L.A., Vernyhorova, Y.V., Popov, S.V., Krijgsman, W., 2017. Middle Miocene paleoenvironmental crises in Central Eurasia caused changes in marine gateway configuration. Glob. Planet. Change 158, 57–71. https://doi.org/10.1016/j.gloplacha.2017.09.013.

Palcu, D.V., Vasiliev, I., Stoica, M., Krijgsman, W., 2019. The end of the great Khersonian drying of Eurasia: magnetostratigraphic dating of the Maeotian transgression in the Eastern Paratethys. Basin Res. 31, 33–58. https://doi.org/10.1111/bre.12307.

Palmer, M.R., Edmond, J.M., 1989. The strontium isotope budget of the modern ocean. Earth Planet. Sci. Lett. 92, 11–26.

Panieri, G., Lugli, S., Manzi, V., Roveri, M., Schreiber, B.C., Palinska, K.A., 2010. Ribosomal RNA gene fragments from fossilized cyanobacteria identified in primary gypsum from the Late Miocene, Italy. Geobiology 8 (2), 101–111. https://doi.org/10.1111/j.1472-4669.2009.00230.x.

Parkhurst, D.L., Appelo, C.A.J., 2013. Description of input and examples for PHREEQC version 3—a computer program for speciation, batch-reaction, one-dimensional transport, and inverse geochemical calculations. In: US Geol. Surv. Tech. Methods, Book 6, p. 497.

Peryt, T.M., 2006. The beginning, development and termination of the Middle Miocene Badenian Salinity Crisis in Central Paratethys. Sediment. Geol. 188–189, 379–396.

Popov, S.V., Rostovtseva, Y.V., Fillippova, N.Y., Golovina, L.A., Radionova, E.P., Goncharova, I.A., Vernyhorova, Y.V., Dykan, N.I., Pinchuk, T.N., Iljina, L.B., Koromyslova, A.V., Kozyrenko, T.M., Nikolaeva, I.A., Viskova, L.A., 2016. Paleontology and stratigraphy of the Middle–Upper Miocene of the Taman Peninsula: part 1. Description of key sections and benthic fossil groups. Paleontol. J. 50, 1–168.

Popov, S.V., Shcherba, I.G., Ilyina, L.B., Nevesskaya, L.A., Paramonova, N.P., Khondkarian, S.O., Magyar, I., 2006. Late Miocene to Pliocene palaeogeography of the Paratethys and its relation to the Mediterranean. Palaeogeogr. Palaeoclimatol. Palaeoecol. 238, 91–106. https://doi.org/10.1016/j.palaeo.2006.03.020.

Raitzsch, M., Dueñas-Bohórquez, A., Reichart, G.-J., de Nooijer, L.J., Bickert, T., 2010. Incorporation of Mg and Sr in calcite of cultured benthic foraminifera: impact of calcium concentration and associated calcite saturation state. Biogeosciences 7, 869–881.

Reghizzi, M., Gennari, R., Douville, E., Lugli, S., Manzi, V., Montagna, P., Roveri, M., Sierro, F.J., Taviani, M., 2017. Isotope stratigraphy (^{87}Sr/^{86}Sr, $δ^{18}$O, $δ13$C) of the Sorbas basin (Betic Cordillera, Spain): paleoceanographic evolution across the onset of the Messinian salinity crisis. Palaeogeogr. Palaeoclimatol. Palaeoecol. 469, 60–73. https://doi.org/10.1016/j.palaeo.2016.12.039.

Reghizzi, M., Lugli, S., Manzi, V., Rossi, F.P., Roveri, M., 2018. Orbitally forced hydrological balance during the Messinian Salinity Crisis: insights from strontium isotopes (^{87}Sr/^{86}Sr) in the Vena del Gesso Basin (Northern Apennines, Italy). Paleoceanogr. Paleoclimatol. 33, 716–731. https://doi.org/10.1029/2018PA003395.

Roveri, M., Flecker, R., Krijgsman, W., Lofi, J., Lugli, S., Manzi, V., Sierro, F.J., Bertini, A., Camerlenghi, A., De Lange, G., Govers, R., Hilgen, F., Hübscher, C., Meijer, P.T., Stoica, M., 2014a. The Messinian Salinity Crisis: past and future of a great challenge for marine sciences. Mar. Geol. 352, 25–58. https://doi.org/10.1016/j.margeo.2014.02.002.

Roveri, M., Lugli, S., Manzi, V., Gennari, R., Schreiber, B.C., 2014b. High-resolution strontium isotope stratigraphy of the Messinian deep Mediterranean basins: implications for marginal to central basins correlation. Mar. Geol. 349, 113–125. https://doi.org/10.1016/j.margeo.2014.01.002.

Ryan, W.B.F., 2009. Decoding the Mediterranean salinity crisis. Sedimentology 56, 95–136. https://doi.org/10.1111/j.1365-3091.2008.01031.x.

Stoica, M., Krijgsman, W., Fortuin, A., Gliozzi, E., 2016. Paratethyan ostracods in the Spanish Lago-Mare: more evidence for interbasinal exchange at high Mediterranean sea level. Palaeogeogr. Palaeoclimatol. Palaeoecol. 441, 854–870. https://doi.org/10.1016/j.palaeo.2015.10.034.

Sun, J., Wang, L., Yu, G., 2015. Effects of Na, Ca, Mg, and Al chloride salts on dissolution and phase stability of calcium sulfate dihydrate in aqueous solutions at 278.15 K to 308.15 K. J. Chem. Eng. Data 60, 2559–2566.

Topper, R.P.M., Lugli, S., Manzi, V., Roveri, M., Meijer, P.T., 2014. Precessional control of Sr ratios in marginal basins during the Messinian Salinity Crisis? Geochem. Geophys. Geosyst. 15, 1926–1944.

Topper, R.P.M., Meijer, P.T., 2013. A modelling perspective on spatial and temporal variations in Messinian evaporite deposits. Mar. Geol. 336, 44–60.

Vai, G.B., Ricci Lucchi, F., 1977. Algal crusts, autochthonous and clastic gypsum in a cannibalistic evaporite basin; a case history from the Messinian of Northern Apennine. Sedimentology 24, 211–244. https://doi.org/10.1111/j.1365-3091.1977.tb00255.x.

Van Baak, C.G.C., Krijgsman, W., Magyar, I., Sztanó, O., Golovina, L.A., Grothe, A., Hoyle, T.M., Mandic, O., Patina, I.S., Popov, S.V., Radionova, E.P., Stoica, M., Vasiliev, I., 2017. Paratethys response to the Messinian salinity crisis. Earth-Sci. Rev. 172, 193–223. https://doi.org/10.1016/j.earscirev.2017.07.015.

Van Baak, C.G.C., Radionova, E.P., Golovina, L.A., Raffi, I., Kuiper, K.F., Vasiliev, I., Krijgsman, W., 2015. Messinian events in the Black Sea. Terra Nova 27. https://doi.org/10.1111/ter.12177.

Van Baak, C.G.C., Stoica, M., Grothe, A., Aliyeva, E., Krijgsman, W., 2016. Mediterranean-Paratethys connectivity during the Messinian salinity crisis: the Pontian of Azerbaijan. Glob. Planet. Change 141, 63–81. https://doi.org/10.1016/j.gloplacha.2016.04.005.

Vasiliev, I., Iosifidi, A.G., Khramov, A.N., Krijgsman, W., Kuiper, K., Langereis, C.G., Popov, V.V., Stoica, M., Tomsha, V.A., Yudin, S.V., 2011. Magnetostratigraphy and radio-isotope dating of upper Miocene-lower Pliocene sedimentary successions of the Black Sea Basin (Taman Peninsula, Russia). Palaeogeogr. Palaeoclimatol. Palaeoecol. 310, 163–175. https://doi.org/10.1016/j.palaeo.2011.06.022.

Vasiliev, I., Karakitsios, V., Bouloubassi, I., Agiadi, K., Kontakiotis, G., Antonarakou, A., et al., 2019. Large sea surface temperature, salinity, and productivity-preservation changes preceding the onset of the Messinian Salinity Crisis in the eastern Mediterranean Sea. Paleoceanogr. Paleoclimatol. 34, 182–202. https://doi.org/10.1029/2018PA003438.

Vasiliev, I., Reichart, G.-J., Davies, G.R., Krijgsman, W., Stoica, M., 2010. Strontium isotope ratios of the Eastern Paratethys during the Mio-Pliocene transition; implications for interbasinal connectivity. Earth Planet. Sci. Lett. 292, 123–131. https://doi.org/10.1016/j.epsl.2010.01.027.

Vasiliev, I., Reichart, G.-J., Krijgsman, W., 2013. Impact of the Messinian Salinity Crisis on Black Sea hydrology-insights from hydrogen isotopes analysis on biomarkers. Earth Planet. Sci. Lett. 362, 272–282. https://doi.org/10.1016/j.epsl.2012.11.038.

Vonhof, H.B., Wesselingh, F.B., Kaandorp, R.J.G., Davies, G.R., van Hinte, J.E., Guerrero, J., Räsänen, M., Romero-Pittman, L., Ranzi, A., 2003. Paleogeography of Miocene Western Amazonia: isotopic composition of molluscan shells constrains the influence of marine incursions. GSA Bull. 115, 983–993.

Warren, J.K., 2010. Evaporites through time: tectonic, climatic and eustatic controls in marine and nonmarine deposits. Earth-Sci. Rev. 98, 217–268. https://doi.org/10.1016/j.earscirev.2009.11.004.